International Journal of Multiphase Flow 150 (2022) 104000

Contents lists available at ScienceDirect

International Journal of Multiphase Flow

journal homepage: www.elsevier.com/locate/ijmulflow

Passive scalar transfer rate at bubble interface in Carreau liquid in a transition regime

Koorosh Kazemi, Anton Vernet, Francesc X. Grau, Salvatore Cito *, Alexandre Fabregat

Department of Mechanical Engineering, Universitat Rovira i Virgili, Av. Països Catalans 26, 43007, Tarragona, Spain

ARTICLE INFO

Keywords:
Bubble rising
Newtonian fluid
Shear thinning fluid
Shear thickening fluid
Mass transfer

ABSTRACT

The scalar transfer rate from a bubble to a quiescent fluid with Carreau rheological behavior is studied here with Bond and Galilei number values respectively equal to 30 and 2 and a non-dimensional inelastic time constant (λ) equal to 6. Under these conditions the bubble dynamics regime stays within the steady and oscillatory areas. Navier Stokes equations are solved numerically in a non-stationary three dimensional domain and are coupled to the mass transfer equation of a scalar. The effect of the Peclet number (Pe) and flow index (n) of the quiescent fluid on the Sherwood number is explored within the following range: $10 < Pe < 1000$, and $0.3 < n < 1.7$. We observed that the shear thinning rheology destabilizes the bubble flow dynamics from steady towards an oscillatory regime and increases transfer rates between the bubble and surrounding fluids. This trend became even more prominent as Pe increased. Our results are condensed into an empirical predictive correlation that outperforms previous similar correlations and can be used to estimate the heat and mass transfer rate at the bubble interface in a Carreau liquid in a transition regime at a specific Galilei and Bond numbers.

1. Introduction

The transfer rate between a bubble and the surrounding fluid is relevant to many applications in the chemical, biochemical and processing industries, as well as in physiological bio-fluids, the pharmaceutical industry, wastewater treatments, bioreactors, and lubrication systems (Chhabra and Richardson, 1999, 2008; Yang et al., 2007; Tavlarides et al., 1970; Chhabra, 2007). Although carrier fluids are often described as Newtonian, most of the aforementioned applications deal with non-Newtonian fluids that exhibit shear thinning or shear thickening behaviors (Pont et al., 2012; Benchabane and Karim, 2008; Ding et al., 2011). When there are temperature or concentration differences between the carrier and dispersed phases, the scalar transfers across the gas–liquid interface. This is a very common phenomenon in a vast number of chemical engineering processes of extraction and distillation as well as in biochemical reactions, including oxidation, cell culture, wastewater treatment and fermentation. Therefore, a thorough knowledge of the transfer rate at the bubble interface in non-Newtonian fluids is of paramount importance (Bao et al., 2020).

Baird and Davidson (1962) experimentally measured the absorption rate of carbon dioxide from single rising bubbles into water. Bischof et al. (1991) developed a novel technique for determining the mass transfer rate in individual air bubbles rising in water. Ponoth and McLaughlin (2000) numerically simulated axisymmetric rising bubbles in aqueous solutions of surfactants and derived correlations for the Sherwood number, the bubble size and Reynolds number. Feng and Michaelides (2001) studied the mass transfer processes in axisymmetric viscous droplets in Newtonian fluid using a finite-difference scheme. These authors reported the results on the dependence of the Sherwood number on the Peclet number (ranging from 1 to 10^3) and the Reynolds number (ranging from 1 to 5×10^2). Saboni et al. (2007) numerically investigated the effects of the viscosity ratio on the mass transfer of an axisymmetric bubble rising in water. They derived a correlation between the surface-average Sherwood number and the Reynolds and Peclet numbers over the 1–400 and 0–10^6 ranges respectively. Huang and Saito (2017) experimentally studied carbon dioxide dissolution in zig-zagging single bubbles in aqueous media and discussed the impact of water contamination on the mass transfer rate.

Although many multiphase flow applications of interest with interfacial transport involve liquid carrier phases exhibiting non-Newtonian behavior, such as polypropylene solutions (Marcovich et al., 2004; Wang et al., 2020), little information is available on the impact of complex rheologies on the dispersed phase dynamics and scalar transfer rate. Exceptions include the work of Barnett et al. (1966) who experimentally studied the carbon dioxide transfer in aqueous (Newtonian)

* Corresponding author.
E-mail addresses: koorosh.kazemi@urv.cat (K. Kazemi), anton.vernet@urv.cat (A. Vernet), francescxavier.grau@urv.cat (F.X. Grau), salvatore.cito@urv.cat (S. Cito), alexandre.fabregat@urv.cat (A. Fabregat).

https://doi.org/10.1016/j.ijmultiphaseflow.2022.104000
Received 17 September 2021; Received in revised form 30 December 2021; Accepted 25 January 2022
Available online 19 February 2022

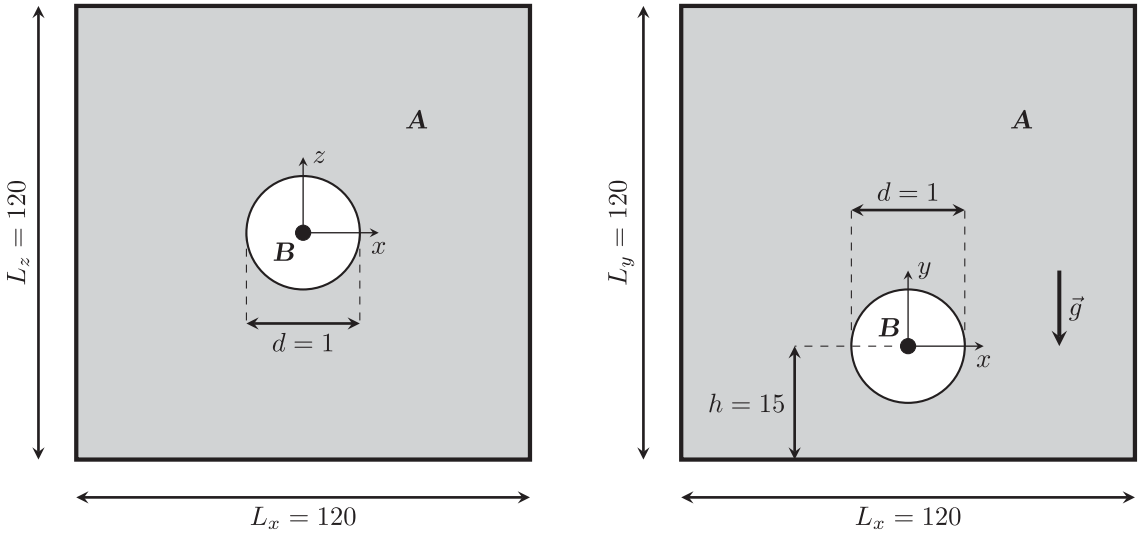

Fig. 1. Top and side views of the computational domain (not to scale) showing the flow configuration with an initially spherical bubble of fluid B and non-dimensional diameter $d = 1$ placed at $y = h = 15$ in a $L_x = L_y = L_z = 120$ cubical box filled with fluid A.

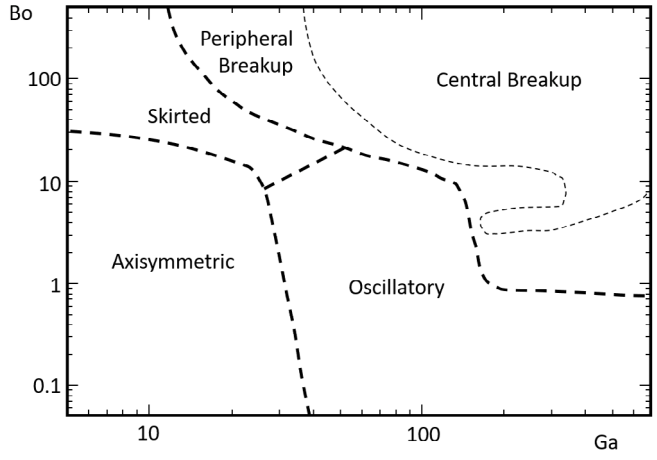

Fig. 2. $Ga - Bo$ phase plot of an air bubble rising in water.
Source: This figure is taken from Tripathi et al. (2015).

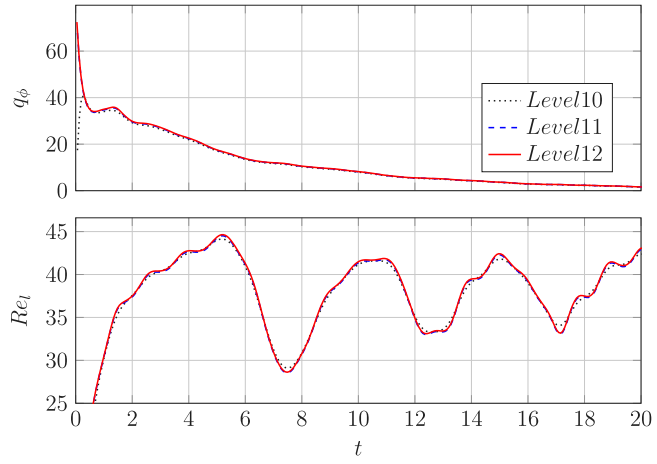

Fig. 3. Non-dimensional density flux and local Reynolds number versus time for different mesh levels, $n = 0.3$ and $Pe = 1000$.

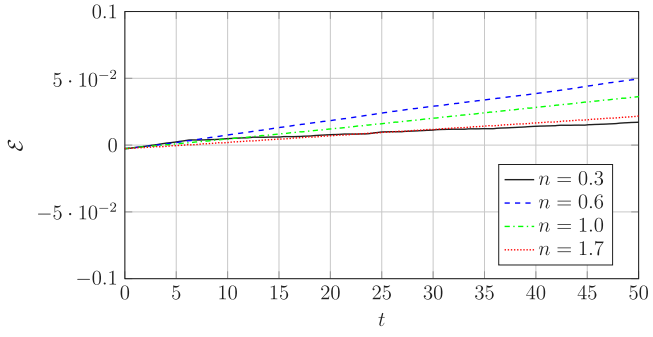

Fig. 4. The mass conservation error versus time.

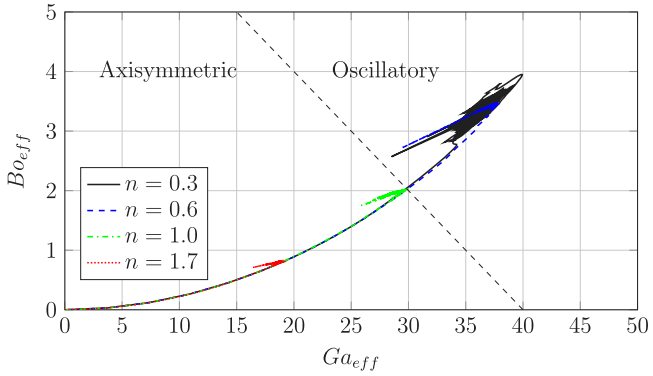

Fig. 5. $Ga - Bo$ phase plot history for different flow indexes.

environments and carboxymethyl cellulose (CMC) solutions (shear thinning), demonstrating that the rheology can affect both the drag and mass transfer coefficients. Using perturbation methods, Bhavaraju et al. (1978) researched the dependence of the Sherwood number in single bubble systems under creeping flow regime using power law ambient fluids and derived correlations for the mass transfer coefficient.

Assuming a spherical bubble and steady and fully developed conditions, Kishore et al. (2007) numerically studied the effects of the Reynolds and Peclet numbers as well as the flow index on the mass transfer in power-law fluids. The results allowed them to predict the effects of these parameters on the surface-average Sherwood number

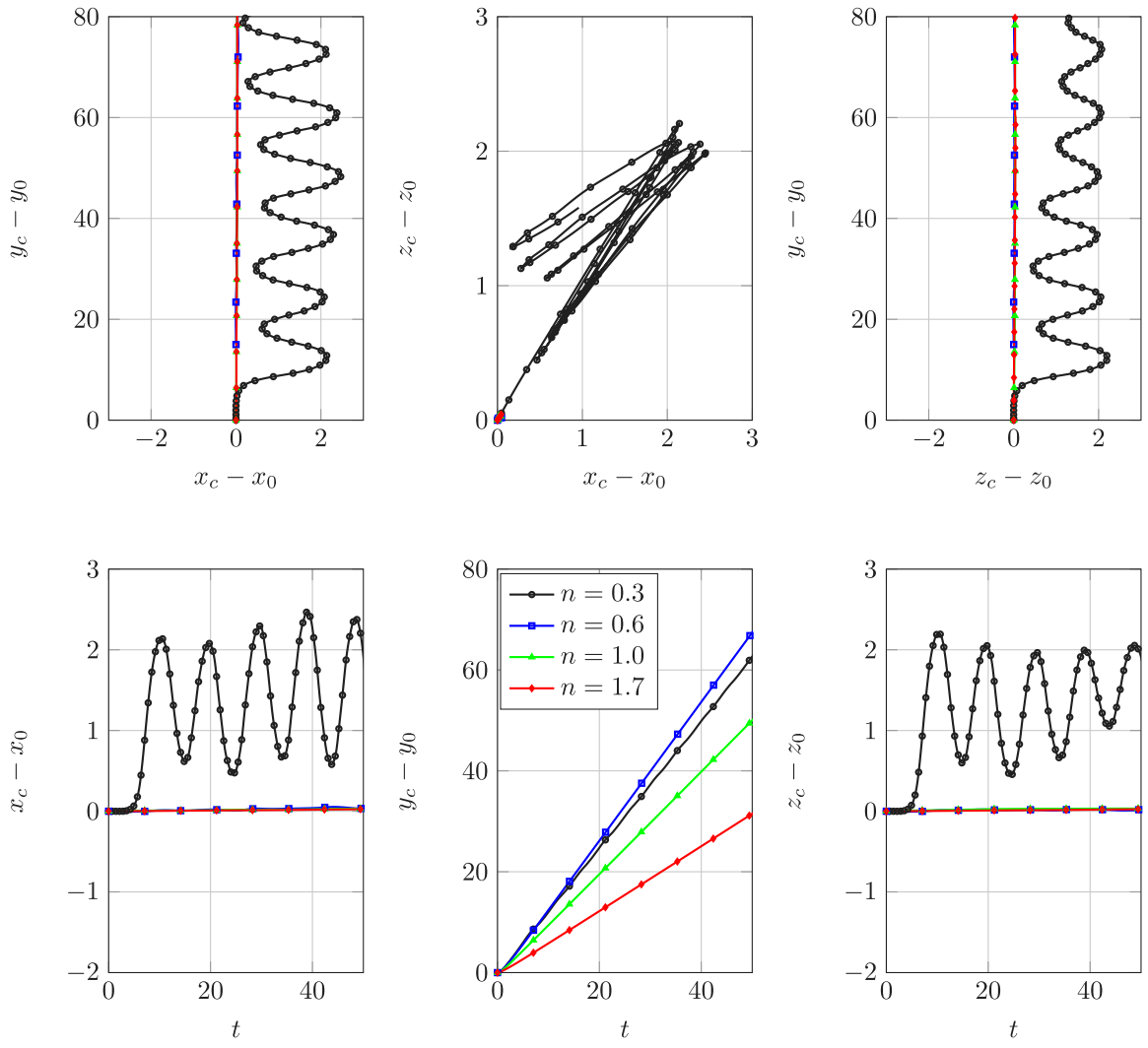

Fig. 6. Bubble trajectory for different flow indexes; top: 2D position of the bubble on each slice, and bottom: coordinates of the bubble versus time.

for moderate Reynolds numbers. Power-law fluids were also considered (Dhole et al., 2007) in their study of the Sherwood number dependence of the Reynolds and Peclet numbers under the axisymmetric steady flow assumption. Assuming steady mass transfer, Cao et al. (2020a) used numerical simulations of a rising bubble in two dimensional yield stress fluids to derive a correction factor to improve the prediction of surface-averaged Sherwood numbers. Similar efforts for improving the Sherwood number estimation were carried out by Vasconcelos et al. (2002) and Gómez-Díaz et al. (2007) who used potential flows at large Reynolds numbers with completely mobile surfaces. Clift et al. (1978) presented a correlation for the Sherwood number for spherical bubbles over a large range of regimes covering from creeping flow to high Reynolds numbers. Also under the potential flow assumption, Coppus and Rietema (1980) introduced a correlation for the mass transfer coefficient in spherical cap bubbles. Spherical cap bubbles were also studied by Kendoush (1994, 2007). They presented a Sherwood number correlations under forced convection and extended the analysis to ellipsoidal bubbles in potential flows.

Few numerical studies that deal with mass transfer from the bubble rising within non-Newtonian fluids assume a spherical bubble under steady conditions. In this study, we propose extending this study of the transfer rate at the bubble interface, including a non-spherical bubble shape, rising in Carreau liquids in a transient regime. Although the Carreau model is widely used for shear thinning fluids, this model has been applied to shear thickening fluids as well (Ahmed et al., 2020; Lashgari et al., 2012; Coclite et al., 2020).

2. Physical model

Fig. 1 shows a diagram of the numerical domain consisting a cubic box filled with Newtonian or non-Newtonian fluids with a length of 120. The radius of the spherical bubble is 0.5 and is initially released at $(x_0, y_0, z_0) = (0, 15, 0)$ with zero velocity. The large box dimensions ensure that the wall effects on the bubble dynamics are minimized.

Using the interface topology, the different regimes of the air–water system are illustrated in a Ga–Bo phase plot in Fig. 2. According to the plot, the five regimes are axisymmetric, oscillatory (zigzag or spiral), skirted, peripheral breakup and central breakup regions (Tripathi et al., 2015). To study the impact of the rheology on the bubble dynamics, the Bond and Galilei numbers were set to $Bo = 2$ and $Ga^0 = 30$. Located very close to the limit with the oscillatory regime, we expected to observe departures from the axisymmetric trajectory exhibited by the air bubble when it is released in water, which is a Newtonian fluid. The values of λ and n for the shear thinning fluids used in this paper are taken from the experiments of Zhang et al. (2010) and also numerical simulation of Premlata et al. (2017). Moreover, we use a value of flow index for shear thickening fluids to study this case as well.

3. Mathematical model

3.1. The non-dimensionalization of the Navier–Stokes Equations for two-phase flows

The mass continuity equation and the momentum or Navier–Stokes Equations (NSE) for incompressible binary and immiscible flows can be written as (Gueyffier et al., 1999):

$$\nabla \cdot \tilde{\mathbf{u}} = 0 \tag{1}$$

$$\rho\left[\frac{\partial \tilde{\mathbf{u}}}{\partial \tilde{t}} + \tilde{\mathbf{u}} \cdot \nabla \tilde{\mathbf{u}}\right] = -\nabla \tilde{p} + \nabla \cdot (\mu \nabla \tilde{\mathbf{u}}) + \delta \sigma \tilde{\kappa} \vec{\mathbf{n}} - \rho g \boldsymbol{\jmath} \tag{2}$$

where $\tilde{\mathbf{u}}(\tilde{u}, \tilde{v}, \tilde{w})$ is the velocity vector with components $\tilde{u}$, $\tilde{v}$ and $\tilde{w}$ aligned in the $\tilde{x}$, $\tilde{y}$ and $\tilde{z}$ directions, respectively. ρ, $\tilde{t}$, $\tilde{p}$, g and μ represent density, time, pressure, gravitational acceleration and dynamic viscosity, respectively. The Dirac delta function, δ, expresses the fact that the surface tension term is concentrated on the interface. σ denotes surface tension coefficient which is constant. $\vec{\mathbf{n}}$ represents the outward-pointing unit normal to the fluid "A" at the interface, $\tilde{\kappa}\vec{\mathbf{n}}$ denotes interfacial curvature and $\boldsymbol{\jmath}$ is the unit vector in the vertical direction (along gravity-negative y direction). The tilde indicates dimensional variables. Here, the surface tension force is considered as a body force term using the continuum method suggested by Brackbill et al. (1992).

Note that, using the Einstein notation, the momentum diffusive term can be expressed in terms of the deformation tensor $D_{ij} = \left(\partial_i u_j + \partial_j u_i\right)/2$ as $\nabla \cdot (\mu \nabla \tilde{\mathbf{u}}) = \nabla \cdot \left(2\mu D_{ij}\right)$.

For two-phase flows, the density and viscosity can be written as:

$$\rho \equiv \rho(f) = \rho_A f + \rho_B (1 - f) \tag{3}$$

$$\mu \equiv \mu(f) = \mu_A f + \mu_B (1 - f). \tag{4}$$

where A stands for the ambient fluid phase (with density ρ_A and dynamic viscosity μ_A) in which its rheology is characterized using the Carreau model and B refers to the bubble fluid (with density ρ_B and dynamic viscosity μ_B) of Newtonian behavior. The volume fraction of fluid f, bounded between 0 (fluid B) and 1 (fluid A), is used to track the interface between two phases.

The velocity, length and pressure scales can be defined as:

$$l^* = R \tag{5}$$

$$u^* = \sqrt{gR} \tag{6}$$

$$p^* = \rho_A (u^*)^2 \tag{7}$$

where R represents the radius of the initially spherical bubble. In this case, the set of non-dimensional parameters yield:

$$Ga = \frac{\rho_A u^* l^*}{\mu_A} = \frac{g^{1/2} R^{3/2}}{\nu_A} \tag{8}$$

$$Bo = \frac{\rho_A u^{*2} l^*}{\sigma} = \frac{\rho_A g R^2}{\sigma} \tag{9}$$

$$Ri = \frac{g l^*}{u^{*2}} = \frac{gR}{gR} = 1 \tag{10}$$

where Ga, Bo and Ri are Galilei, Bond and Richardson numbers, respectively.

The non-dimensional governing Navier–Stokes equations can be written as:

$$\frac{D\mathbf{u}}{Dt} = \frac{1}{\alpha}\left[-\nabla p + \frac{1}{Ga}\nabla \cdot (\beta \nabla \mathbf{u}) + \frac{1}{Bo}\delta \kappa \vec{\mathbf{n}}\right] - \boldsymbol{\jmath} \tag{11}$$

where $\alpha = \frac{\rho}{\rho_A} = f + \rho^\star(1 - f)$, $\beta = \frac{\mu}{\mu_A} = f + \mu^\star(1 - f)$ and the density and dynamic viscosity ratios are defined as $\rho^\star = \frac{\rho_B}{\rho_A}$ and $\mu^\star = \frac{\mu_B}{\mu_A}$, respectively.

3.2. Non-Newtonian model

For a non-Newtonian surrounding fluid (fluid A), the viscosity is dependent of the shear rate. The Carreau rheological model can be written as (Yasuda et al., 1981):

$$\mu_A = \mu_A^0 \eta = \mu_A^0 \left[1 + (\lambda \Pi)^2\right]^{(n-1)/2}. \tag{12}$$

where μ_A^0 represents the dynamic viscosity of fluid A corresponding to the zero shear rate. λ and n are the inelastic time constant and flow index, respectively. $\Pi = (E_{ij} E_{ij})^{0.5}$ is the second invariant of the strain rate tensor, wherein $E_{ij} = \frac{1}{2}\left(\frac{\partial u_i}{\partial x_j} + \frac{\partial u_j}{\partial x_i}\right)$.

Using the scaling already described, we finally obtain the non-dimensional NSE for the bubble rising in Newtonian/non-Newtonian fluids as:

$$\frac{D\mathbf{u}}{Dt} = \frac{1}{\alpha}\left[-\nabla p + \frac{1}{Ga^0}\nabla \cdot (\beta \nabla \mathbf{u}) + \frac{1}{Bo}\delta \kappa \vec{\mathbf{n}}\right] - \boldsymbol{\jmath} \tag{13}$$

where the $Ga^0 = \frac{\rho_A g^{1/2} R^{3/2}}{\mu_A^0}$, $\beta = \frac{\mu}{\mu_A^0}$ and $\mu^\star = \frac{\mu_B}{\mu_A^0}$. In this study, the density ratio, $\rho^\star$, and the initial viscosity ratio, $\mu^\star$, are set to 0.001 and 0.01, respectively.

3.3. Passive scalar transport

The general equation for the transport of a passive scalar ϕ can be written as:

$$\frac{\partial \tilde{\phi}}{\partial \tilde{t}} + \nabla \cdot \tilde{\mathbf{u}}\tilde{\phi} = \nabla \cdot \left(D \nabla \tilde{\phi}\right) \tag{14}$$

where D is the passive scalar diffusion coefficient.

The equation above can be non-dimensionalized using $\phi = (\tilde{\phi} - \tilde{\phi}_\infty)/(\tilde{\phi}_0 - \tilde{\phi}_\infty)$ where $\tilde{\phi}_0$ and $\tilde{\phi}_\infty$ are the initial scalar within the bubble and far-field values, respectively. Thus, the non-dimensional equation reads:

$$\frac{\partial \phi}{\partial t} + \nabla \cdot \mathbf{u}\phi = \frac{1}{Pe}\nabla^2 \phi \tag{15}$$

where $Pe = \frac{u^* l^*}{D}$ is Peclet number. Initial value of ϕ inside the bubble is 1 and everywhere else is zero.

The density flux of the scalar $\tilde{\phi}$ can be written as:

$$q_\phi'' = -D \nabla \tilde{\phi} \tag{16}$$

where D is the scalar diffusion coefficient.

This quantity can also be expressed using Newton's Law of Cooling as:

$$q_\phi'' = h_\phi \left(\tilde{\phi}_s - \tilde{\phi}_\infty\right). \tag{17}$$

where h_ϕ is the local convective transport coefficient, $\tilde{\phi}_s$ is the local value of $\tilde{\phi}$ at the bubble surface and $\tilde{\phi}_\infty$ is the environment value of the scalar (assumed constant).

The amount of $\tilde{\phi}$ transferred from the bubble to the environment through the interface $\tilde{S}(\tilde{t})$ can be written as:

$$\widetilde{q_\phi} = \frac{\partial}{\partial \tilde{t}}\int_{\tilde{\mathcal{V}}} \tilde{\phi} d\tilde{\mathcal{V}} = \int_{\tilde{S}} -D \nabla \tilde{\phi} \cdot \vec{\mathbf{n}} d\tilde{S} = \int_{\tilde{S}} h_\phi \left(\tilde{\phi}_s - \tilde{\phi}_\infty\right) d\tilde{S} \tag{18}$$

where $\tilde{\mathcal{V}}(\tilde{t})$ is the bubble volume (assumed constant). Using the Gauss Theorem, the non-dimensional form of the Eq. (18) can be written as:

$$\frac{\widetilde{q_\phi}}{l^* \phi^* D} = q_\phi = Pe \frac{\partial}{\partial t}\int_{\mathcal{V}} \phi d\mathcal{V} = -\int_{\mathcal{V}} \nabla^2 \phi d\mathcal{V} = \int_S \frac{h_\phi l^*}{D}\phi_s dS \tag{19}$$

Using $\langle\rangle$ to denote interface averaged quantities, $\langle h_\phi \rangle$ is the surface-averaged convective transport coefficient and $\langle \phi_s \rangle$ is the surface-averaged value of ϕ, and Eq. (19) can be written as:

$$\langle Sh \rangle = \frac{q_\phi}{\langle \phi_s \rangle} = -\frac{\int_V \nabla^2 \phi dV}{\langle \phi_s \rangle} = \frac{l^* \langle h_\phi \rangle}{D} \tag{20}$$

And therefore,

$$q_\phi = \langle Sh \rangle \langle \phi_s \rangle \tag{21}$$

where $\langle Sh \rangle$ is the surface-averaged Sherwood number.

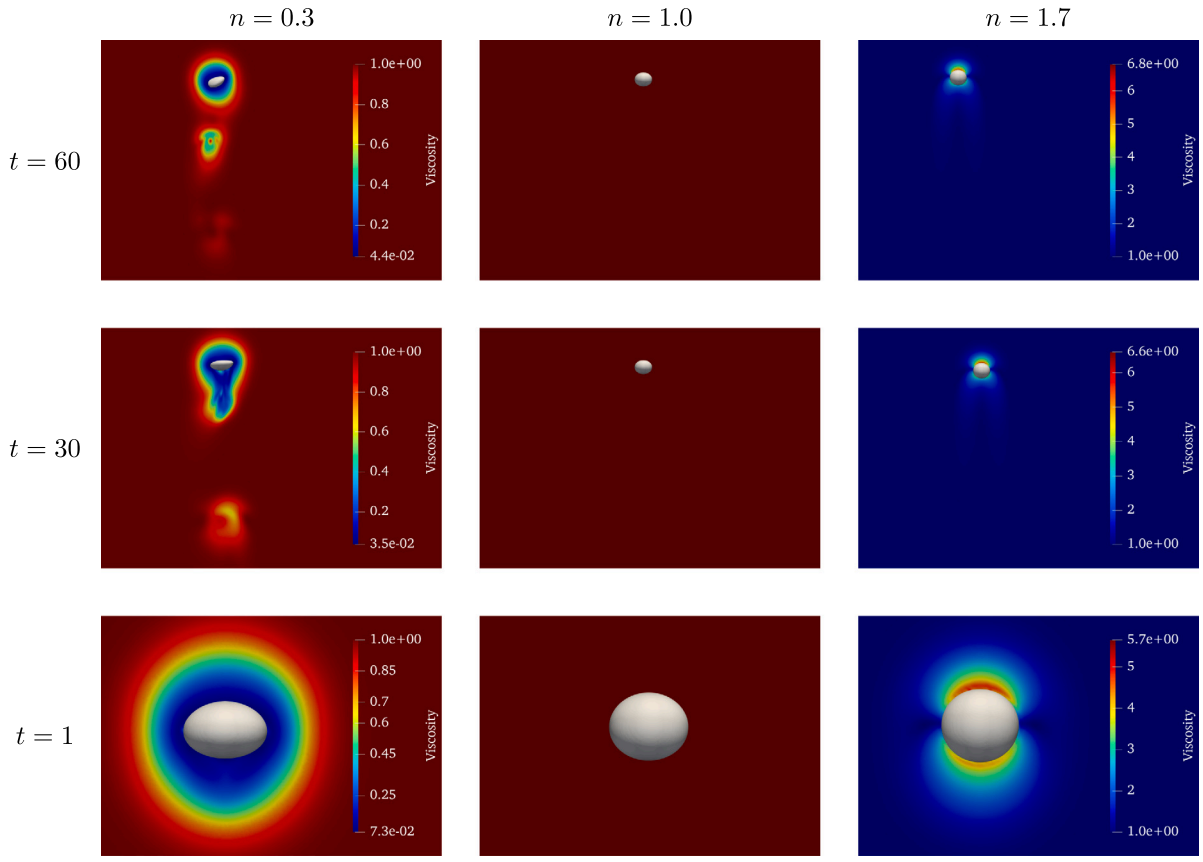

Fig. 7. Viscosity profiles, μ, for different flow indexes at different times in y–z plane.

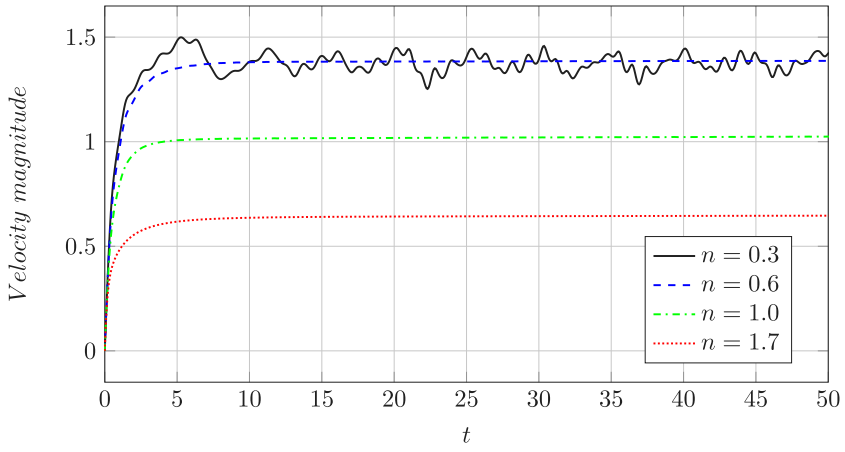

Fig. 8. Velocity magnitude versus time for different flow indexes.

3.4. Numerical method

Eqs. (1), (13) and (15) are solved using *Basilisk* (Popinet, 2019), a Volume-of-Fluid (VOF) open source solver widely used to numerically investigate multiphase flows (Karnakov et al., 2020; López-Herrera et al., 2019). *Basilisk* uses a surface-tracking approach to numerically study the evolution of complex interfaces that eventually can breakup and/or coalesce under large density and viscosity ratios. Using balanced-force continuum surface force formulation to calculate the surface tension force, *Basilisk* guarantees the minimization of parasitic currents at the interface (Popinet, 2009). Numerical efficiency is ensured by dynamically increasing the local mesh resolution according to user-specified criteria. In the present application, the oct-tree based mesh refinement strategy uses local values of velocity magnitude and the passive scalar concentration along with the bubble interface position by controlling the error on them. Different tank volumes were compared to identify the optimal domain size that ensured that the effects of the walls, modeled as no-slip surfaces, are negligible. Under the oct-tree mesh hierarchy used in the solver, the background mesh resolution level was set to refinement level 2^5 which corresponds to a mesh resolution of 32 cells in each direction. The mesh refinement strategy resulted in an increase in the total number of cells of up to 10^7 cells. Using the temporal evolution of the non-dimensional density flux q_ϕ and local Reynolds number $Re_l = \frac{\rho_A u_b d}{\mu_A^0}$ where u_b is the bubble rising velocity and d is initial diameter of the bubble, mesh-independence results for $n = 0.3$ and $Pe = 1000$ are shown in Fig. 3.

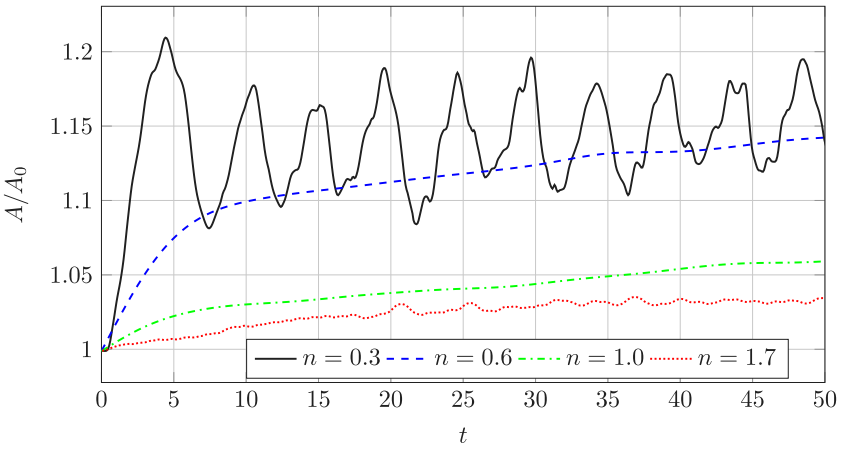

Fig. 9. Bubble area ratio versus time for different flow indexes.

The differences between the three different considered mesh levels, $m = 10, 11, 12$, suggest that $m = 11$ leads to satisfactory grid resolutions. Mesh level, m, indicates the level of refinement applied to the initial mesh resolution based on the different parameters (here, local values of velocity magnitude, the passive scalar concentration and bubble interface position). In addition, the mass conservation error is defined as the variation in the bubble volume:

$$\mathcal{E} = 100\frac{\mathcal{V}(t) - \mathcal{V}_0}{\mathcal{V}_0} \tag{22}$$

where $\mathcal{V}_0$ is the initial volume of the bubble and $\mathcal{V}(t) = (1-f)\int_V dV(t)$. Fig. 4 shows that the error is under 0.05% for all simulations. Note that negligible differences are observed between the different cases in Fig. 4. These differences are mainly due to the use of adaptive mesh refinement, which implies a different mesh resolution for each case. The open source *Basilisk* code has been modified to account for rheological effects and compute the transfer rate directly without any further post processing. The procedure of calculating q_ϕ by using volume integral inside the bubble and the Carreau rheological model are added to the Basilisk as well as the surface-averaged value of the scalar, $\langle \phi_s \rangle$, which is necessary to calculate $\langle Sh \rangle$.

4. Results

We simulated a single bubble rising in Newtonian, shear thinning and shear thickening fluids in a large tank and studied the effects of the rheological properties on the bubble dynamics and the effects of the Peclet number and rheological properties on the mass transfer across the bubble interface.

4.1. Effects of the rheological properties on the behavior of the bubble rising dynamics

The bubble rising dynamics behavior strongly depends on the rheological properties such as the flow index. Defining effective Galilei number, $Ga_{eff} = \frac{\rho_A u_b L}{\mu_A}$ and effective Bond number, $Bo_{eff} = \frac{\rho_A {u_b}^2 L}{\sigma}$, where u_b is the bubble rising velocity and characteristic length scale is $L = V/A$, we can see the effects of the flow index on $Ga-Bo$ phase plot in Fig. 5. It can be seen that for the shear thickening case, the bubble dynamics behavior shifts to the axisymmetric region while for the shear thinning cases it shifts to the oscillatory region.

In this section, we studied the effects of the flow index on the bubble rising dynamics, which includes bubble trajectory, rising velocity, shape of the bubble and the viscosity field. Four different flow indexes, n, were considered: 0.3 and 0.6 for the shear thinning fluids, 1 for the Newtonian fluid and 1.7 for the shear thickening fluid.

4.1.1. Bubble trajectory

Fig. 6 shows the position of the center of mass of the bubble initially located at $(x_0 = 0, y_0 = 15, z_0 = 0)$ versus time for different cases. The results indicate that the bubble rises along the vertical axis for $n = 1.0$ and also for $n = 0.6$ and $= 1.7$. In contrast, the most extreme case of shear thinning, with $n = 0.3$, shows an oscillatory path characterized by a zigzag motion. As a result, this case exhibits larger bubble excursions and lateral departures. This suggests that when the background flow behaves as a shear-thinning fluid, the bubble dynamics may eventually resemble those exhibited by a Newtonian ambient fluid at larger Galilei numbers. Moreover, by zooming into Fig. 6, one can find that when $n = 0.3$, the bubble rises faster in comparison with the case of $n = 0.6$ until $t = 0.5$ when the oscillatory behavior of the bubble starts to grow up.

4.1.2. Interface topology

Fig. 7 shows $x = 0$ slices of the viscosity field for different flow indexes at three different times along with the shape of the bubble (in white). In comparison to $n = 1$, shear thinning ambient fluids lead to significant departures from the spherical shape of the bubble which tends to flatten as it rises. In contrast, shear thickening ambient fluid tends to prevent the bubble from significant deformation. When growing in a shear thinning fluid, the oscillatory behavior of the bubble in Fig. 6 also results in oscillatory changes in the bubble topology. In contrast, changes in the bubble shape are slight for $n = 0.6, 1.0, 1.7$. This is clearly observed in both Fig. 8 and Fig. 9 which show respectively the temporal evolution of rising velocity magnitude of the bubble and the normalized bubble interface area. When compared to the Newtonian case, shear thickening ambient fluid leads to a significantly lower rising velocity due to locally increased viscous friction. On the other hand, reduced viscosity in the interface vicinity leads to faster rising bubbles for both $n = 0.6$ and $n = 0.3$. In the latter case, however, the bubble exhibits an oscillatory behavior with a vertical rise velocity mean value very close to the constant value exhibited by the $n = 0.6$ case.

Note that instead of using a bubble shape factor, measuring based on the maximum and minimum characteristics length, to track the evolution of the interface growth as in Gumulya et al. (2019) and Cao et al. (2020b), the results in Fig. 9 use the actual normalized bubble interface area. The definition proposed in here is more accurate since we can explicitly measure the bubble surface area. The rate of bubble interface deformation for the Newtonian, the $n = 0.6$ and the $n = 1.7$ cases, rapidly saturates and remains almost constant along the duration of the numerical experiment. In contrast, despite its oscillatory behavior, the interface area in the $n = 0.3$ case seems to grow at a slower rate in comparison to the other cases. Taking the fast Fourier transform of the bubble area, the velocity of the bubble in y-direction and velocity magnitude versus time for the case $n = 0.3$, the main frequency for the bubble area and the velocity of the bubble in y-direction is 0.2 while for the velocity magnitude is 0.4.

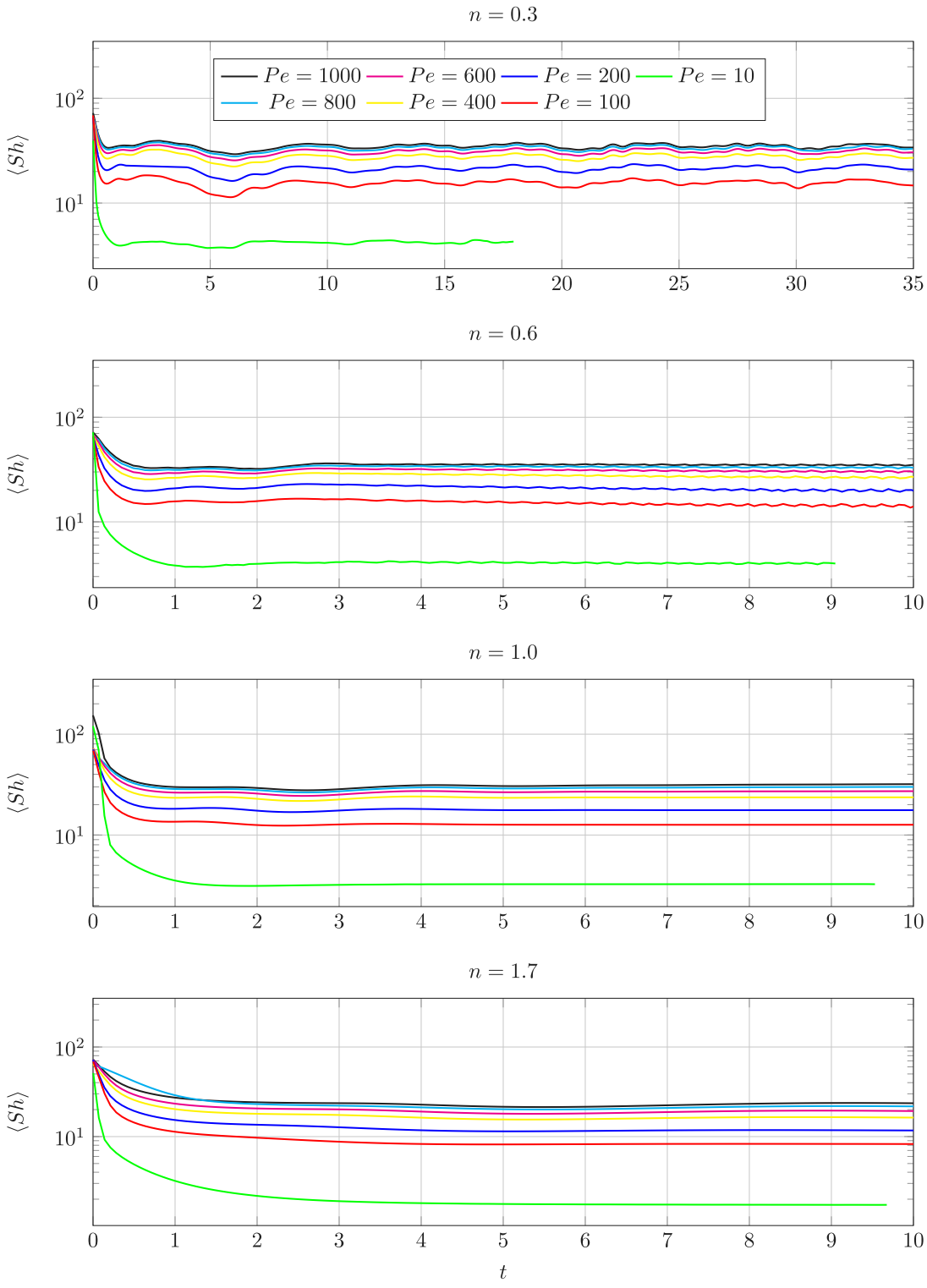

Fig. 10. Surface-averaged Sherwood number vs. time for different Peclet numbers and flow indexes.

4.2. Effects of the rheological properties and Peclet number on the mass transfer between the bubble and surrounding liquid

In this section, the effects of the flow index and Peclet number on the mass transfer across the bubble interface are studied. In addition to the previous flow indexes, seven different Peclet numbers are also considered: 10, 100, 200, 400, 600, 800 and 1000. Fig. 10 shows the surface-averaged Sherwood number versus time for different Peclet numbers and flow indexes. It can be seen that for $n = 1$ and $n = 1.7$, the surface-averaged Sherwood number reaches a constant value while for the shear thinning cases, it oscillates over time. The oscillatory behavior of the surface-averaged Sherwood number in shear thinning fluids is due to the oscillatory behavior of the rising velocity of the bubble and time-dependent behavior of the diameter of the bubble. Taking the fast Fourier transform of the surface-averaged Sherwood number versus time, the main frequency for the surface-averaged Sherwood number for the case $n = 0.3$ is 0.2, which is equal to the frequency of the bubble rising velocity in y-direction as well as the frequency of the bubble area.

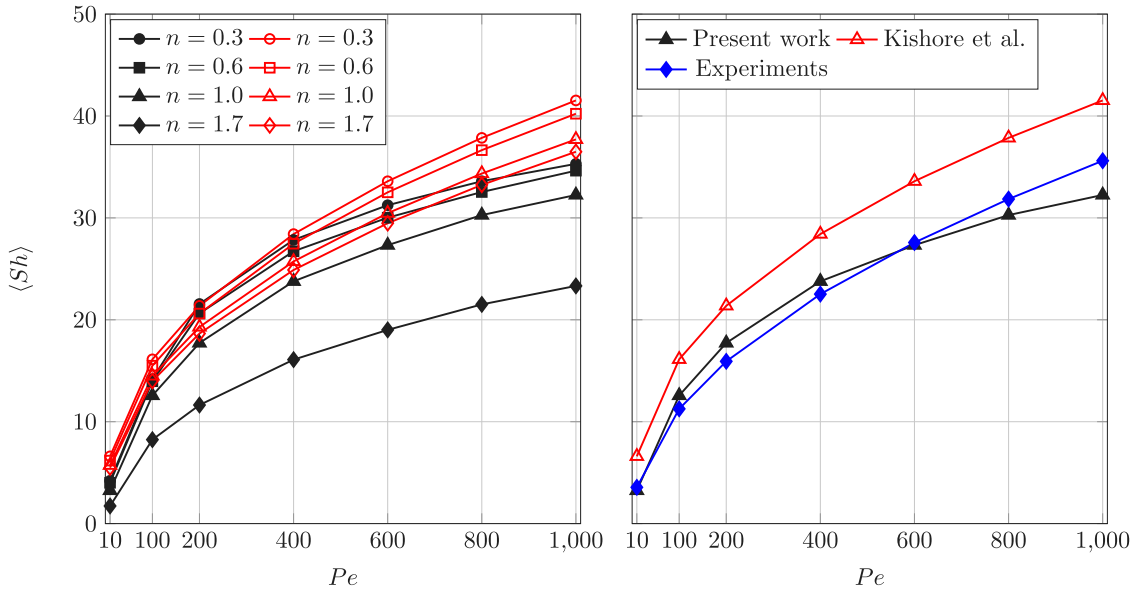

Fig. 11. Surface-averaged Sherwood number versus Peclet number. Left panel: Comparison of the present study (black) and Kishore et al. (2007) (red) for several flow indexes. Right panel: comparison to experimental results for $n = 1.0$. (For interpretation of the references to color in this figure legend, the reader is referred to the web version of this article.)

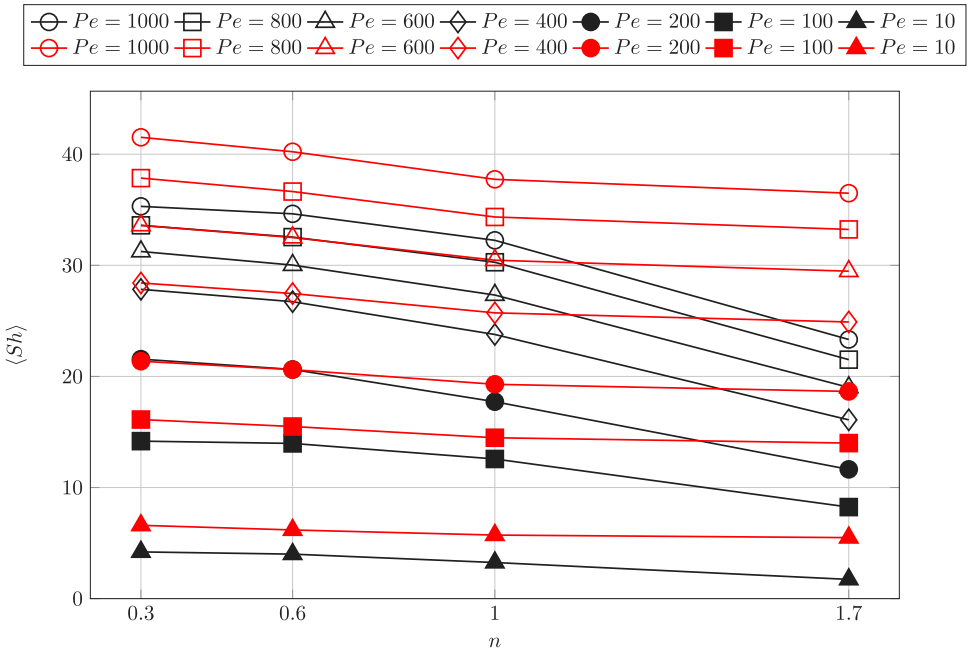

Fig. 12. Surface-averaged Sherwood number versus flow index for different Peclet numbers. Present study and Kishore et al. (2007) results in black and red, respectively. (For interpretation of the references to color in this figure legend, the reader is referred to the web version of this article.)

To have a constant value for the surface-averaged Sherwood number in the shear thinning cases, the time averaged value of $\langle Sh \rangle$ is calculated.

Kishore et al. (2007) presented a correlation for the average Sherwood number for the mass transfer between a fluid sphere and power-law liquids. They considered an oversimplified model with a spherical and rigid drop moving steadily in an infinite two dimensional power-law fluid medium with the constant drop size in spite of the mass transfer between two phases so that they could use quasi-steady state assumptions. Therefore, they developed a correlation for the average Sherwood number as a function of the Reynolds number, Peclet number, flow index and viscosity ratio with the assumptions of a quasi-steady state, which means that the mass transfers steadily from the fluid sphere to the surrounding fluid. In other words, they assumed that the quantity of the scalar inside the bubble is always constant. This correlation is as follow:

$$\langle Sh \rangle = \left[\frac{1.19(n+1)}{1.7n+1.5}\right] Re_A^{0.53} \left(\frac{Pe}{Re_A}\right)^{0.42} (\mu^\star)^{-0.14} + \left(\frac{n+1}{1.5n}\right) Pe^{-0.15} (\mu^\star)^{0.25}. \tag{23}$$

The surface-averaged Sherwood number obtained in the present study is compared with the averaged Sherwood number calculated by Kishore et al. (2007) in Fig. 11 (left) and with the experimental results of Roudet et al. (2017) for the Newtonian case in Fig. 11 (right). It can be seen that our results are in good agreement with the experimental ones. The differences between our results and Kishore's results

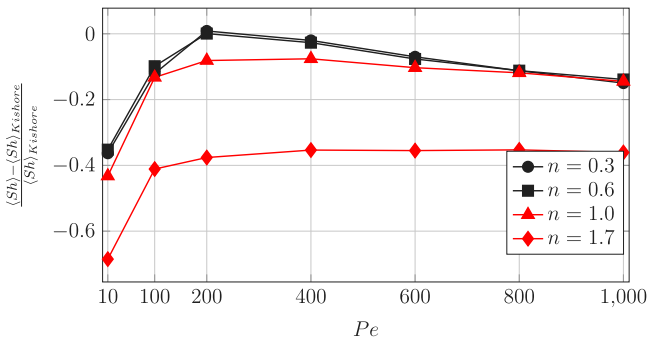

Fig. 13. Sherwood number deviation.

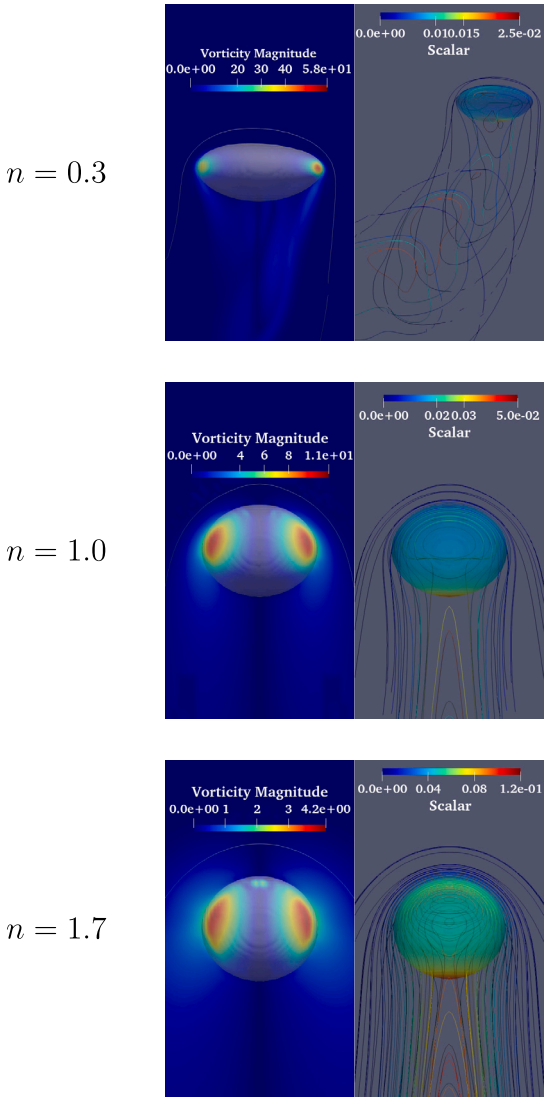

Fig. 14. Scalar field, ϕ, and vorticity field for different flow indexes at $t = 10$ in y–z plane, $Pe = 100$.

are due to the different conditions: they considered an axisymmetric undeformable liquid drop with a constant scalar value inside the bubble located in an infinite power-law fluid, while we have a deformable gas bubble that rises in Newtonian and non-Newtonian fluids modeled with the Carreau and the value of the scalar inside the bubble is not constant. These differences are shown in Fig. 12, comparing the surface-averaged Sherwood number versus flow index for different Peclet numbers with the results of Kishore et al. (2007). In addition, Fig. 13 indicates the differences between our results and the results of Kishore et al. (2007) for the averaged Sherwood number versus Peclet number for different flow indexes.

Fig. 14 shows the vorticity and isolines for the scalar around the bubble for different flow indexes at $t = 10$. It can be seen that there are two main vortices inside the bubble and their magnitudes increase with a decreasing flow index, while their covered areas decrease. Moreover, it can be seen that the thickness of the scalar boundary layer increases by increasing the flow index while the complexity and 3D effects decrease. Furthermore, it can be seen that by decreasing the flow index, the scalar diffuses faster. This increase in transfer rate is caused by the increase of bubble velocity and surface area and therefore an increase in convection around the bubble. In non-Newtonian cases, investigated in this article, the strain-rate tensor strongly affects the local deformation of the fluid interfaces. Vela-Martín and Avila (2021) showed that the local variation of the surface energy depends on the strain rate tensor. Here, we observe that the strain rate tensor strongly affects the local deformation of the fluid interfaces (Fig. 9). In shear thinning fluids the velocity gradients are bigger which lead to more deformation while in shear thickening fluids the deformation is less due to the smaller values of the velocity gradients. Here, strain-rate tensor magnitude at the interface for shear thinning fluids is greater than the magnitude for shear thickening fluids.

A simple correlation for the surface-averaged Sherwood number can be developed (Guimerà et al., 2020) based on the present numerical results. This correlation can estimate the rate of mass transfer in a gas–liquid system in which a deformable bubble rises in Newtonian and non-Newtonian ambient fluids:

$$\langle Sh\rangle = 2.15 \ln\left(\frac{Pe}{n^n}\right) \qquad \begin{matrix} 0.3 \le n \le 1.7 \\ 10 \le Pe \le 1000 \end{matrix} . \tag{24}$$

Fig. 15, shows non-dimensional density flux, q_ϕ, versus time for different ambient fluids and different Peclet numbers.

As it can be seen in Fig. 15, the logarithmic non-dimensional density flux depends linearly on time for $t > 2$. A simple correlation for the non-dimensional density flux can be developed to estimate the flux in a gas–liquid system for different ambient fluids and Peclet numbers. The following expression was extracted from the present numerical results:

$$q_\phi = 2.24\langle Sh\rangle \left[\frac{\langle Sh\rangle}{Pe}\left(119.0 + \langle Sh\rangle + \frac{33.35}{n}\right)\right]^{-0.11(0.067+t)} \qquad \begin{matrix} 0.3 \le n \le 1.7 \\ 10 \le Pe \le 1000 \\ 0 \le \langle Sh\rangle \le 40 \end{matrix} \tag{25}$$

5. Discussion

This work numerically simulates a single bubble rising in a large tank to study the effects of the rheological properties on the bubble dynamics and mass transfer from the bubble to the surrounding fluids. For the given parameters, the bubble rises vertically on the center line of the cavity in the Newtonian fluids. By decreasing the flow index (shear thinning), the rising velocity of the bubble increases and as a result, the local Ga number increases and the bubble trajectory changes to the zigzag motion, which means that the behavior of the bubble dynamics shifts to the oscillatory region in Fig. 2. And vice versa, increasing the flow index (shear thickening) leads to decrease the rising velocity and local Ga number so that the behavior of the bubble dynamics shifts to the axisymmetric region.

The increase of the local viscosity in shear thickening fluids leads to a reduction of the momentum diffusion, the smoothing of the local velocity gradients and, therefore, the reduction of the rate of strain. As a result, the interface deformation is not remarkable, the bubble

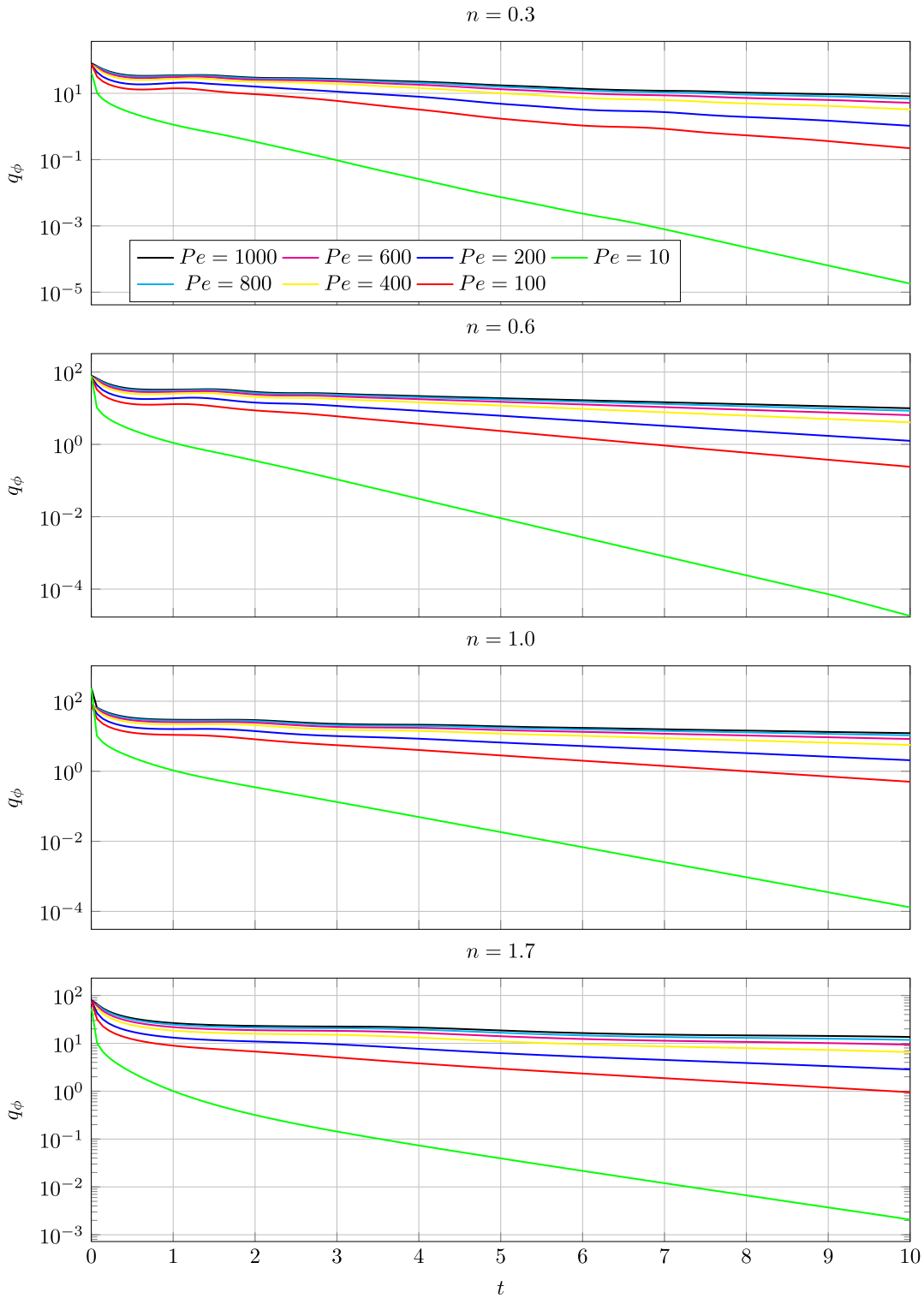

Fig. 15. Non-dimensional density flux vs. time for different Peclet numbers and flow indexes.

remains almost spherical and the area of the bubble increases slightly. By decreasing the flow index, the local viscosity in the vicinity of the bubble decreases leading to an increase in the momentum diffusion, local velocity gradients and as a result, an increase in the rate of strain. Therefore, the bubble deforms more and the area of the bubble increases. Increasing the area as well as the rising velocity of the bubble leads to faster mass transfer from the bubble to the ambient fluid.

At low Pe numbers, the effects of the flow index on the surface-averaged Sherwood number is really small. At high Pe numbers, the surface-averaged Sherwood number increases by decreasing the flow index which means that the mass transfer is more inefficient at higher flow indexes. Concentration contours show that the scalar boundary layer thickness around the bubble increases by decreasing the flow index. Moreover, the complexity and 3D effects increase by decreasing

the flow index due to the oscillatory behavior and deformation of the bubble.

Since the scalar value inside the bubble diffuses, we are able to capture the density flux. Together with the surface-averaged Sherwood number, density flux is a crucial parameter for displaying the efficiency of the mass transfer in a transient state. Density flux increases by decreasing the flow index, which leads to the more efficient mass transfer at lower flow indexes.

6. Conclusions

A single gas bubble rising in a Newtonian fluid, a shear thinning fluid and a shear thickening fluid were simulated numerically using *Basilisk* with adaptive mesh refinement based on the velocity magnitude, passive scalar value and the position of the interface to study the effects of the flow index on the bubble dynamics and mass transfer rate across the interface for different Peclet numbers. For the shear thickening fluid, the rising velocity is relatively low and the shape of the bubble does not deform, while by decreasing the flow index, the rising velocity and the deformation of the bubble increase. For the shear thinning fluid, the surface-averaged Sherwood number has an oscillatory behavior versus time due to the oscillatory behavior of the rising velocity magnitude. In this work, we considered the effects of the deformation of the bubble, the 3D dynamics behavior and a non-constant scalar value inside the bubble on the mass transfer rate. We found a correlation for surface-averaged Sherwood number as a function of the Peclet number and flow index and a correlation for density flux as a function of the surface-averaged Sherwood number, Peclet number, flow index and time.

CRediT authorship contribution statement

Koorosh Kazemi: Conceptualization, Methodology, Software, Validation, Investigation, Writing – original draft. **Anton Vernet:** Conceptualization, Methodology, Supervision, Writing – review & editing. **Francesc X. Grau:** Conceptualization, Methodology, Supervision, Writing – review & editing. **Salvatore Cito:** Conceptualization, Methodology, Supervision, Writing – review & editing, Funding acquisition. **Alexandre Fabregat:** Conceptualization, Methodology, Supervision, Writing – review & editing, Funding acquisition.

Declaration of competing interest

The authors declare that they have no known competing financial interests or personal relationships that could have appeared to influence the work reported in this paper.

Acknowledgments

This work was funded by the Spanish Ministerio de Ciencia, Innovación y Universidades through the grants DPI2016-75791-C2-1-P and RTI2018-100907-A-I00 (MCIU/AEI/FEDER, UE) and also by the Generalitat de Catalunya through the grant 2017-SGR-1234.

We thank Professor Jordi Pallarés for his comments and suggestions during the preparation of this manuscript preparation. We also thank the Red Española de Supercomputación (RES) for the computational resources used for some of the simulations presented here under project ID IM-2021-1-0008.

References

Ahmed, B., Hayat, T., Alsaedi, A., Abbasi, F.M., 2020. Entropy generation analysis for peristaltic motion of carreau–yasuda nanomaterial. Phys. Scr. 95 (5), 055804.
Baird, M., Davidson, J., 1962. Gas absorption by large rising bubbles. Chem. Eng. Sci. 17 (2), 87–93.
Bao, Y., Jia, J., Tong, S., Gao, Z., Cai, Z., 2020. A review on single bubble gas-liquid mass transfer. Chin. J. Chem. Eng..
Barnett, S.M., Humphrey, A.E., Litt, M., 1966. Bubble motion and mass transfer in non-Newtonian fluids. AIChE J. 12 (2), 253–259.
Benchabane, A., Karim, B., 2008. Rheological properties of carboxymethyl cellulose (CMC) solutions. Colloid Polym. Sci. 286, 1173–1180.
Bhavaraju, S.M., Mashelkar, R.A., Blanch, H.W., 1978. Bubble motion and mass transfer in non-Newtonian fluids: Part I. Single bubble in power law and bingham fluids. AIChE J. 24 (6), 1063–1070.
Bischof, F., Sommerfeld, M., Durst, F., 1991. The determination of mass transfer rates from individual small bubbles. Chem. Eng. Sci. 46 (12), 3115–3121.
Brackbill, J., Kothe, D., Zemach, C., 1992. A continuum method for modeling surface tension. J. Comput. Phys. 100 (2), 335–354.
Cao, B., Fan, J., Sun, X., Li, S., 2020a. Numerical simulation of mass-transfer characteristics of a bubble rising in yield stress fluids. ACS Omega 5 (23), 13878–13885.
Cao, Y., Mateos Canals, I., Macián-Juan, R., 2020b. Path instability of a compressible air bubble rising in quiescent water with consideration of variable thermophysical properties. Int. J. Multiph. Flow. 129, 103320.
Chhabra, R., 2007. Chapter 1 - introduction. In: Chhabra, R. (Ed.), Bubbles, Drops, and Particles in Non-Newtonian Fluids, second ed. Boca Raton, CRC Press, pp. 1–8.
Chhabra, R., Richardson, J., 1999. Chapter 1 - non-Newtonian fluid behaviour. In: Chhabra, R., Richardson, J. (Eds.), Non-Newtonian Flow in the Process Industries. Butterworth-Heinemann, Oxford, pp. 1–36.
Chhabra, R., Richardson, J., 2008. Chapter 1 - non-Newtonian fluid behaviour. In: Chhabra, R., Richardson, J. (Eds.), Non-Newtonian Flow and Applied Rheology (Second Edition), second ed. Butterworth-Heinemann, Oxford, pp. 1–55.
Clift, R., Grace, J., Weber, M., 1978. Bubbles, drops, and particles.
Coclite, A., Coclite, G.M., De Tommasi, D., 2020. Capsules rheology inCarreau–Yasuda fluids. Nanomaterials 10 (11).
Coppus, J., Rietema, K., 1980. Theoretical derivation of the mass transfer coefficient at the front of a spherical cap bubble. Chem. Eng. Sci. 35 (6), 1497–1499.
Dhole, S., Chhabra, R., Eswaran, V., 2007. Mass transfer from a spherical bubble rising in power-law fluids at intermediate Reynolds numbers. Int. Commun. Heat Mass Transfer 34, 971–978.
Ding, J., Li, W., Shen, S.Z., 2011. Research and applications of shear thickening fluids. Recent Pat. Mater. Sci. 4 (1), 43–49.
Feng, Z.-G., Michaelides, E.E., 2001. Heat and mass transfer coefficients of viscous spheres. Int. J. Heat Mass Transfer 44 (23), 4445–4454.
Gómez-Díaz, D., Gomes, N., Teixeira, J., Belo, I., 2007. Oxygen mass transfer to emulsions in a bubble column contactor. Chem. Eng. J. 152, 354–360.
Gueyffier, D., Li, J., Nadim, A., Scardovelli, R., Zaleski, S., 1999. Volume-of-fluid interface tracking with smoothed surface stress methods for three-dimensional flows. J. Comput. Phys. 152 (2), 423–456.
Guimerà, R., Reichardt, I., Aguilar-Mogas, A., Massucci, F.A., Miranda, M., Pallarès, J., Sales-Pardo, M., 2020. A Bayesian machine scientist to aid in the solution of challenging scientific problems. Sci. Adv. 6 (5).
Gumulya, M., Joshi, J., Utikar, R., Evans, G., Pareek, V., 2019. Characteristics of energy production and dissipation around a bubble rising in water. Chem. Eng. Sci. 193, 38–52.
Huang, J., Saito, T., 2017. Influences of gas–liquid interface contamination on bubble motions, bubble wakes, and instantaneous mass transfer. Chem. Eng. Sci. 157, 182–199.
Karnakov, P., Litvinov, S., Koumoutsakos, P., 2020. A hybrid particle volume-of-fluid method for curvature estimation in multiphase flows. Int. J. Multiph. Flow. 125, 103–209.
Kendoush, A.A., 1994. Theory of convective heat and mass transfer to spherical-cap bubbles. AIChE J. 40 (9), 1440–1448.
Kendoush, A.A., 2007. Heat, mass, and momentum transfer to a rising ellipsoidal bubble. Ind. Eng. Chem. Res. 46 (26), 9232–9237.
Kishore, N., Chhabra, R., Eswaran, V., 2007. Mass transfer from a single fluid sphere to power-law liquids at moderate Reynolds numbers. Chem. Eng. Sci. 62 (21), 6040–6053.
Lashgari, I., Pralits, J.O., Giannetti, F., Brandt, L., 2012. First instability of the flow of shear-thinning and shear-thickening fluids past a circular cylinder. J. Fluid Mech. 701, 201–227.
López-Herrera, J., Popinet, S., Castrejón-Pita, A., 2019. An adaptive solver for viscoelastic incompressible two-phase problems applied to the study of the splashing of weakly viscoelastic droplets. J. Non-Newton. Fluid Mech. 264, 144–158.
Marcovich, N.E., Reboredo, M.M., Kenny, J., Aranguren, M.I., 2004. Rheology of particle suspensions in viscoelastic media. Wood flour-polypropylene melt. Rheol. Acta 43, 1435–1528.
Ponoth, S.S., McLaughlin, J., 2000. Numerical simulation of mass transfer for bubbles in water. Chem. Eng. Sci. 55 (7), 1237–1255.
Pont, G., Chen, L., Spiller, D.G., Adams, D.J., 2012. The effect of polymer additives on the rheological properties of dipeptide hydrogelators. Soft Matter 8, 7797–7802.
Popinet, S., 2009. An accurate adaptive solver for surface-tension-driven interfacial flows. J. Comput. Phys. 228 (16), 5838–5866.
Popinet, S., 2019. Solitary wave run-up on a plane beach. http://basilisk.fr/src/test/beach-ml.c.
Premlata, A.R., Tripathi, M.K., Karri, B., Sahu, K.C., 2017. Numerical and experimental investigations of an air bubble rising in a carreau-yasuda shear-thinning liquid. Phys. Fluids 29 (3), 033103.

Roudet, M., Billet, A.-M., Cazin, S., Risso, F., Roig, V., 2017. Experimental investigation of interfacial mass transfer mechanisms for a confined high-reynolds-number bubble rising in a thin gap. AIChE J. 63 (6), 2394–2408.
Saboni, A., Alexandrova, S., Spasic, A., Gourdon, C., 2007. Effect of the viscosity ratio on mass transfer from a fluid sphere at low to very high peclet numbers. Chem. Eng. Sci. 62 (17), 4742–4750.
Tavlarides, L.L., Coulaloglou, C.A., Zeitlin, M.A., Klinzing, G.E., Gal-Or, B., 1970. Bubble and drop phenomena. Ind. Eng. Chem. 62 (11), 6–27.
Tripathi, M., Sahu, K., Govindarajan, R., 2015. Dynamics of an initially spherical bubble rising in quiescent liquid. Nature Commun. 6, 6268.
Vasconcelos, J.M.T., Orvalho, S.P., Alves, S.a.S., 2002. Gas–liquid mass transfer to single bubbles: Effect of surface contamination. AIChE J. 48 (6), 1145–1154.
Vela-Martín, A., Avila, M., 2021. Deformation of drops by outer eddies in turbulence. J. Fluid Mech. 929, A38.
Wang, S., Chen, K., Xue, P., Jia, M., 2020. Research on the preparation and properties of foamed PP/wood flour composites. Mater. Res. Express 7, 035308.
Yang, G., Du, B., Fan, L., 2007. Bubble formation and dynamics in gas–liquid–solid fluidization—A review. Chem. Eng. Sci. 62 (1), 2–27.
Yasuda, K., Armstrong, R.C., Cohen, R.E., 1981. Shear flow properties of concentrated solutions of linear and star branched polystyrenes. Rheol. Acta 20 (2), 163–178.
Zhang, L., Yang, C., Mao, Z.-S., 2010. Numerical simulation of a bubble rising in shear-thinning fluids. J. Non-Newton. Fluid Mech. 165 (11), 555–567.